

Molybdenum Defect Complexes in Bismuth Vanadate

Enesio Marinho Jr.^{ID*} and Cedric Rocha Leão^{ID†}

Federal University of ABC (UFABC), 09210-580 Santo André, São Paulo, Brazil.

(Dated: March 14, 2024)

Monoclinic bismuth vanadate (BiVO_4) is a promising n -type semiconductor for applications in sunlight-driven water splitting. Several studies have shown that its photocatalytic activity is greatly enhanced by high concentrations of Mo and W dopants. In the present work, we performed *ab initio* calculations to assess the most favorable relative position between Mo-related pairs in BiVO_4 . Surprisingly, we verify that the lowest energy configuration for Mo_V pairwise defects in BiVO_4 occurs on nearest-neighbor sites, despite the higher electrostatic repulsion and larger strain on the crystal lattice. Similar results were observed for W_V defect pairs in W-doped BiVO_4 . We show that the origin of this effect lies in a favorable hybridization between the atomic orbitals of the impurities that is only verified when they are closest to each other, resulting in an enthalpy gain that overcomes the repulsive components of the pair formation energy. As a consequence, Mo and/or W doped BiVO_4 are likely to present donor-donor defect complexes, which is an outcome that can be applied in experimental approaches for improving the photocatalytic activity of these metal oxides.

I. INTRODUCTION

Semiconductor metal oxides have been intensively investigated for photoanodes in photoelectrochemical (PEC) water splitting cells [1]. Promising materials for energy conversion and storage through water splitting must present chemical stability, relatively low cost, suitable band edge positions, high optical absorption, long lived excitations and large carrier drift lengths [2, 3]. Metal oxides are usually resilient to water corrosion and are low cost materials, but also present crucial intrinsic limitations. For example, TiO_2 with a wide band gap has low efficiency in absorbing visible light, Fe_2O_3 despite the moderate band-gap, has unfavorable band edge alignment relative to water's electrolysis potentials [3, 4].

Monoclinic scheelite-type bismuth vanadate (BiVO_4) has emerged as a promising complex metal oxide photoanode, since Kudo *et al.* [5] first reported its high visible light photoactivity. BiVO_4 has been estimated theoretically to have a potential to harvest up to 11% of the solar spectrum, delivering a photocurrent of 7.5 mA/cm^2 , with 9% solar-to-hydrogen conversion efficiency under AM 1.5 sunlight illumination [6]. This owes to BiVO_4 moderate band gap, 2.4–2.5 eV [7, 8] and good band edge's alignment with respect to water's redox potentials. Its conduction band edge is close to 0 V *vs* RHE [3, 9], requiring low applied external bias to drive PEC's hydrogen production.

Despite these promising properties, the experimental performance of pristine BiVO_4 as photoanodes is significantly limited by some key factors, such as short charge carrier diffusion lengths and high electron-hole recombination rate [3, 4, 10].

Different experimental approaches have been adopted to overcome these limiting factors of BiVO_4 , including

crystal morphology control [11], heterojunctions [12, 13], tandem PEC devices [14], coupling with oxygen evolving catalysts [15, 16], and extrinsic doping [17–19].

Doping is possibly the simplest attempt to improve the performance of metal oxides in PECs by supplying additional free carriers. BiVO_4 has been effectively n -type doped with tungsten (W) and molybdenum (Mo) [20, 21]. When Mo^{6+} or W^{6+} is embedded into V^{5+} sites, even at moderate concentrations, the photoelectrochemical performances of the doped BiVO_4 electrodes has been noticeably enhanced [22]. Jeong *et al.* [23] have experimentally demonstrated that there exists an optimal doping concentration of Mo and W in BiVO_4 that maximizes the performance of the photoanode. The reported optimal concentrations are fairly high (8% and 10%, respectively), indicating that a comprehensive study of complexes involving these dopants in BiVO_4 is important to rationalize and potentially enhance their beneficial effects for PEC hydrogen production. Recently, Pakeetood *et al.* [24] have reported that Mo_V defects do show a tendency to group with W_V defects in co-doped material, giving rise to donor-donor complexes. The authors argue that this is an unexpected trend owing to the repulsive coulomb interaction between the donor defects.

In the present work, we studied how Mo-defects interact with each other in a BiVO_4 matrix. Using density functional theory we investigated how the electronic properties of BiVO_4 with pairs of Mo substitutional dopants depend on the relative position between these impurities. Applying the well established formalism of first-principles calculations for point defects in solids, combined with analysis of the electronic properties, we also observe that pairs of Mo-defects present lowest formation energy on nearest-neighbor sites. The formation energy rises for intermediate distance between the dopants and then drops again as they get farther apart. We show that this surprising behavior can be rationalized by competing effects between local lattice strain, electrostatic repulsion, and gain of enthalpic stability through hybridization of the electronic clouds of the de-

* enesio.junior@ufabc.edu.br

† cedric.rocha@ufabc.edu.br

fects achieved at short distances.

II. COMPUTATIONAL DETAILS

Our *ab initio* calculations were based on the density functional theory [25, 26], as implemented in Vienna *ab initio* simulation package (VASP) [27]. The projector augmented wave (PAW) method [28] were used to treat the electron-ion interaction, and the exchange-correlation energy was described by the generalized-gradient approximation (GGA) as proposed by Perdew, Burke, and Ernzerhof (PBE) [29].

Structural optimizations were achieved using conjugate gradient algorithm until the Hellmann-Feynman forces on all atoms reach values lower than or equal to 0.025 eV/Å. Kohn-Sham orbitals were expanded into a plane-wave basis set with a cutoff energy of 500 eV. The Bi 5*d*6*s*6*p*, V 4*s*3*d*, O 2*s*2*p*, and Mo 4*s*4*p*4*d*5*s* electrons were treated as valence electrons.

We consider the base-centered monoclinic primitive cell containing 2 units of BiVO₄ (12 atoms), with symmetry described by the standard space group C2/*c*. The optimized lattice parameters for the conventional unit cell were $a = 7.325$ Å, $b = 11.765$ Å, $c = 5.179$ Å, and $\beta = 135.09^\circ$, which are in good agreement with previous theoretical and experimental reports [18, 30]. To study the Mo-related point defects, we considered a 216-atom supercell which was built up by a $3 \times 3 \times 2$ projection of the BiVO₄ primitive cell. The Brillouin zone was sampled using a Γ -centered $7 \times 7 \times 7$ k -point grid for the structural optimization of the BiVO₄ primitive cell, following the scheme proposed by Monkhorst and Pack [31], and a reduced Γ -centered $3 \times 3 \times 4$ grid was used in the calculations with the 216-atom supercells.

Experimental and theoretical preliminary results have indicated that the Mo substitution in V sites is the most energetically favorable defect configuration for this impurity in BiVO₄ systems [20, 32]. For this reason, we modeled the Mo-related point defects only as substituting Mo in V sites (Mo_V).

First, we studied a single Mo_V defect in BiVO₄. We analyzed the electronic structure and also the equilibrium formation thermodynamics of this point defect, besides the study of the intrinsic point defects considering the Bi, V and O vacancies. Furthermore, we studied these same properties for pairs of Mo_V defect into BiVO₄, examining the influence of the relative distances between substitutional V-sites in the electronic and structural properties, choosing substitutional sites 4 Å, 7 Å, and 10 Å far from the reference site (Fig. 1).

III. RESULTS AND DISCUSSION

The GGA-PBE calculated band structure for the BiVO₄ primitive cell is shown in Fig. 2a. The result

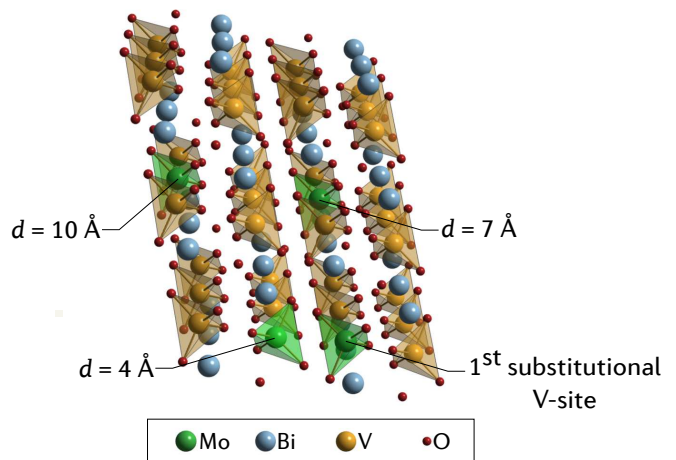


FIG. 1. Representation of the crystal structures of monoclinic BiVO₄ doped with Mo. The green tetrahedrons highlight the V-sites selected for the substitution with Mo atoms. For pair of Mo_V, we considered three relative distances of the substitutional V-sites: 4 Å, 7 Å, and 10 Å far apart from the first V-site.

yields a bandgap of 2.08 eV, which is 0.40 eV underestimated relative to the experimental value [33]. The band gap is indirect with CBM located at the *R* point and the valence-band maximum (VBM) located in the *G-L* direction. The direct gap is about 0.15 eV larger than the indirect gap, in excellent agreement with previous experimental and theoretical reports [8, 9].

Fig. 2b shows the density of states (DOS) of the BiVO₄ primitive cell, projected onto the respective atomic orbitals. Both Bi 6*s* and O 2*p* orbitals contribute to the highest states of the valence band, whereas the V 3*d* orbitals form the states of the bottom of the conduction band. In Fig. 2c, the orbital-resolved DOS of the 216-atom BiVO₄ supercell containing a single Mo_V is shown. The electronic contribution of orbital Mo 4*d* occurs mainly in deep energy levels of the valence band, 7 eV lower than the Fermi energy, and at the bottom of the conduction band. We do not notice significant changes in the shape of the valence and conduction band edges.

Defect formation can be seen as a thermodynamic process in which atoms and electrons are exchanged between the crystal containing point defects and the pristine one which acts as a particle reservoir. The analysis of point defect energies provides some fundamental information about the optoelectronic properties of semiconductors, such as if a certain defect tends to donate electrons to the system, accept electrons or remain neutral in the crystal. The occurrence of deep/shallow energy levels owing to these point defects can also be assessed.

The equilibrium defect concentration is calculated according to a Boltzmann distribution [34]:

$$\frac{n_{\text{eq}}}{N} \approx \exp\left(\frac{-\Delta H_f}{k_B T}\right), \quad (1)$$

where n_{eq} denotes the number of point defects at equi-

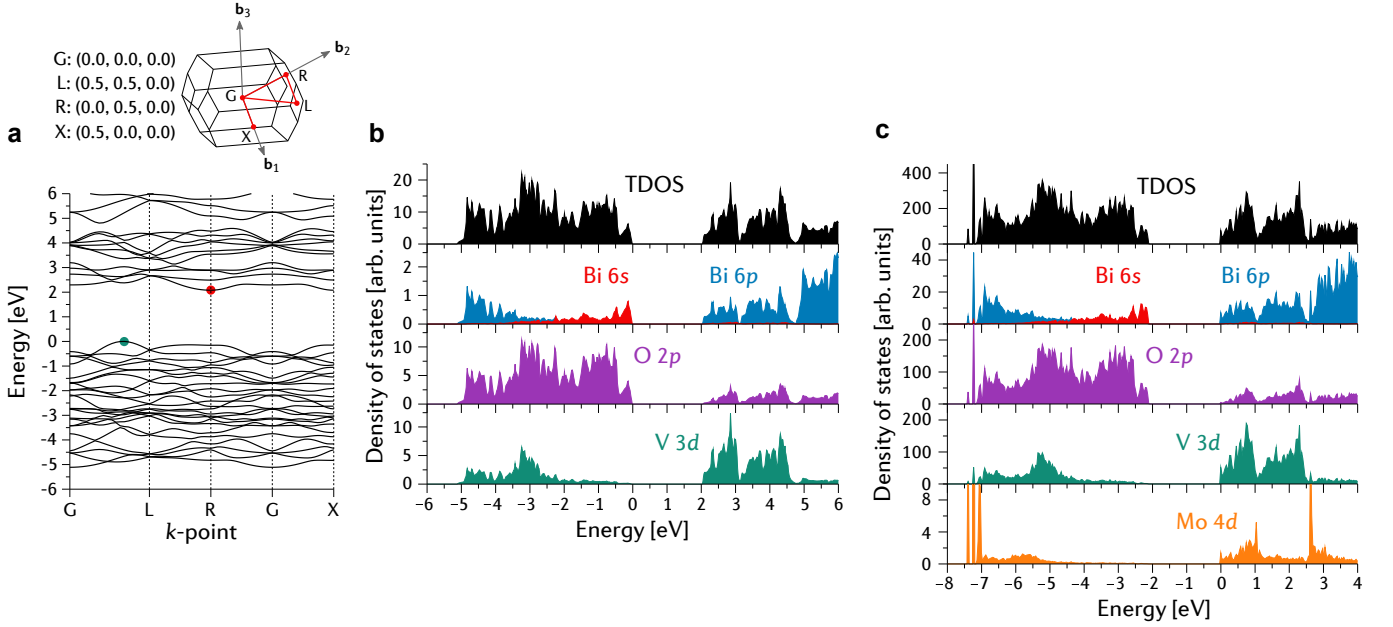


FIG. 2. (a) Electronic band structure and (b) projected density of states of the BiVO_4 primitive cell. Above the band structure, we depicted the selected high symmetry k -points in the Brillouin Zone. In (c), we presented the projected density of states of the 216-atom BiVO_4 supercell with a single Mo_V defect. The Fermi level was used as the zero-energy reference in each plot.

librium, N is the total atomic sites involved in the defect formation, and ΔH_f is the enthalpy of formation.

The formation enthalpy of a point defect in a charge state q is given by

$$\Delta H_f = (E_D - E_p) + \sum_i n_i \mu_i + q(E_v + \mu_e) + E_{\text{corr}}, \quad (2)$$

where E_D and E_p are the total energy of the supercell with the defect and of the pristine supercell, respectively; μ_i is the absolute value of the chemical potential of atom i ; n_i is the number of such defect atoms added ($n < 0$) or removed ($n > 0$); q is the charge state of the defect; μ_e is the chemical potential of the reservoir with which the system exchanges electrons or holes (Fermi level); and E_v is the valence band maximum energy.

Finally, the last term E_{corr} corresponds to the finite size correction, which should be included to remove spurious electrostatic interactions between the charged defect and its periodic images [35, 36]. Makov and Payne [37] (MP) described this correction energy, focusing on cubic cells, as follows:

$$E_{\text{corr}}^{\text{MP}} = \frac{q^2 \alpha_M}{2\epsilon L} - \frac{2\pi q Q}{3\epsilon L^3}, \quad (3)$$

where $L = \Omega^{-1/3}$ is the linear supercell dimension (Ω is the supercell volume), q is the defect charge state, ϵ is the macroscopic dielectric constant of the medium, α_M is the appropriate Madelung constant for the respective supercell geometry, and Q is the second radial moment of the localized charge distribution ρ_c :

$$Q = \int_{V_{\text{sc}}} r^2 \rho_c(\mathbf{r}) d\mathbf{r}. \quad (4)$$

We estimate the leading (first order) correction term in Eq. (3) for 216-atom monoclinic supercells by the Ewald method, computing the Ewald energy (E_{Ewald}) of a point charge (H^+) placed into the supercell of interest and scaling the result by the calculated macroscopic dielectric constant. We obtained $E_{\text{Ewald}} = -1.454$ eV, and the calculated Madelung constant of BiVO_4 supercell was $\alpha_M = 2.8$. Furthermore, while ϵ strictly is a tensor, in our calculations we employed the lowest ϵ diagonal element. For BiVO_4 , our results of dielectric constants were $\epsilon_{xx} = \epsilon_{zz} = 7.24 \epsilon_0$ and $\epsilon_{yy} = 6.04 \epsilon_0$, in good agreement with other theoretical works [18, 38]. Therefore, we adopted $\epsilon = 6.04 \epsilon_0$ in Eq. (3) aiming to apply the upper limit of this correction in the calculation of formation energies.

Lany and Zunger [39, 40] (LZ) have proposed to calculate the second radial moment in Eq. (4) considering that charge difference beyond the vicinity of the defect is predominantly described by a delocalized screening charge of density n_s such that

$$\rho_c \approx n_s = \frac{q}{\Omega} \left(1 - \frac{1}{\epsilon} \right), \quad (5)$$

and therefore the second radial moment could be calculated, substituting Eq. (5) into Eq. (4). For a general geometry, with $a \neq b \neq c$ lattice parameters, we have that $Q = (1/12)(a^2 + b^2 + c^2)$. Using this result in Eq. (4), the image charge correction yields:

$$E_{\text{corr}}^{\text{LZ}} = \left[1 - c_{\text{sh}} \left(1 - \frac{1}{\epsilon} \right) \right] \frac{q^2 \alpha_M}{2\epsilon L} \equiv (1 - f) \frac{q^2 \alpha_M}{2\epsilon L}, \quad (6)$$

in which the term c_{sh} is the so-called shape factor. For

instance, for a cubic cell $c_{\text{sh}} = \pi/3\alpha \approx 0.369$ [35, 40]. For the 216-atom monoclinic supercell of BiVO_4 , we obtain $c_{\text{sh}} = 0.419$, and this higher value was expected due to the anisotropic shape of the monoclinic supercell [40].

Finally, we calculate the image charge correction for 216-atom monoclinic supercell of BiVO_4 , applying the LZ scheme:

$$E_{\text{corr}}^{\text{LZ}} \approx 0.651 \frac{q^2 \alpha_M}{2\epsilon L}, \quad (7)$$

and therefore we verified that although the monoclinic supercell is not approximately isotropic, the computed scaling factor $(1 - f)$ is in excellent agreement with $(1 - f) \approx 2/3$ proposed by Lany and Zunger for systems approximately isotropic and with large macroscopic dielectric constants [39, 40].

To the thermodynamic study of the point defects, we considered as intrinsic defects the vacancies of Bi (V_{Bi}), V (V_{V}) and O (V_{O}), and the extrinsic point defect considered was the Mo substitutional on V site (Mo_V).

Defect formation energies are conventionally defined with respect to the chemical potential of the elemental solid, as shown by Eq. (2). Numerical values of the atomic chemical potentials depend on the stoichiometric conditions under which the defects are created. In order to assure the stable growth of the desired compound, we must impose fundamental thermodynamic conditions to equilibrium chemical potentials, as detailed below [41]:

- (i.) To avoid precipitation of the atomic phases, the chemical potential of the atoms available to the crystal growth (the so-called *atomic chemical potential*) should be smaller than the chemical potential of the respective elemental bulk or gas. That is:

$$\Delta\mu_{\text{Bi,V,O}} \equiv \mu_{\text{Bi,V,O}} - \mu_{\text{Bi,V,O}}^{\text{bulk/gas}} \leq 0. \quad (8)$$

- (ii.) To maintain the thermodynamic stability of the BiVO_4 crystal growth, the sum of the $\Delta\mu$ of the reacting elements must be equal to the heat of formation of BiVO_4 :

$$\Delta H_{\text{BiVO}_4} = \Delta\mu_{\text{Bi}} + \Delta\mu_{\text{V}} + 4\Delta\mu_{\text{O}}, \quad (9)$$

where this heat of formation can be described as follows:

$$\Delta H_{\text{BiVO}_4} = \mu_{\text{BiVO}_4}^{\text{bulk}} - [\mu_{\text{Bi}}^{\text{bulk}} + \mu_{\text{V}}^{\text{bulk}} + 4\mu_{\text{O}}^{\text{gas}}], \quad (10)$$

and each of these terms can be calculated by first-principles approach given the following definition of chemical potential:

$$\mu^{\text{bulk/gas}} = \frac{E_{\text{total}}}{N_{\text{formulas}}}. \quad (11)$$

- (iii.) The chemical potentials are further restricted by requiring that other possible competing phases are

not formed. In the present work, we considered the following competing phases: Bi_2O_3 , V_2O_5 and VO_2 , as proposed in the Refs. [18] and [20]. Thus, we have that

$$2\Delta\mu_{\text{Bi}} + 3\Delta\mu_{\text{O}} \leq \Delta H_{\text{Bi}_2\text{O}_3}, \quad (12)$$

$$\Delta\mu_{\text{V}} + 2\Delta\mu_{\text{O}} \leq \Delta H_{\text{VO}_2}, \quad (13)$$

$$2\Delta\mu_{\text{V}} + 5\Delta\mu_{\text{O}} \leq \Delta H_{\text{V}_2\text{O}_5}. \quad (14)$$

- (iv.) Additional constraints must be posed to avoid the possible formation of compounds containing Mo and the forming elements of the host material. We have considered the following additional competing phases: MoO_2 , and MoO_3 :

$$\Delta\mu_{\text{Mo}} + 2\Delta\mu_{\text{O}} \leq \Delta H_{\text{MoO}_2}, \quad (15)$$

$$\Delta\mu_{\text{Mo}} + 3\Delta\mu_{\text{O}} \leq \Delta H_{\text{MoO}_3}. \quad (16)$$

Applying the thermodynamic constraints described in Eqs. (8)-(16), we achieved the accessible range for the atomic chemical potentials of Bi, V, and O, which is depicted by the shaded area in the Fig. 3a. The formation energies of the vacancies and Mo-related point defects in BiVO_4 were calculated using Eq. (2), considering the conditions “A” (O-poor condition) (Fig. 3b) and “B” (O-rich condition). Figs. 3b and 3c show that the energies needed to form V_{Bi} and V_{V} are higher than that to form V_{O} , when E_{F} is close to the top of the valence band (VBM). These differences tend to decrease considerably when E_{F} is bordering the conduction band (CBM). This is in agreement with the fact that the highest valence band states are constituted mostly from O 2p orbitals, and the bottom of the conduction band is formed by V 3d states. In addition, V_{Bi} and V_{V} defects tend to be negatively charged throughout most of the allowed range Fermi level can assume. V_{O} defects tend to be positively charged. For this reason, V_{Bi} and V_{V} can be described as hole-producing acceptors, and V_{O} are electron-producing donors to the crystal.

The position of the electronic state introduced by the defects relative to the band edges of the host material can be estimated by the transition energy $\epsilon(q/q')$, which is defined as the Fermi energy at which the charge state of a given defect spontaneously transforms from q to q' [41]. The transition energies of the analyzed point defects in BiVO_4 are shown in Table I. These results were obtained based on the formation energy curves represented in Figs. 3b and 3c. V_{Bi} and V_{V} defects are both deep acceptors, which means that their ionization energies are significantly above the thermal energy $k_{\text{B}}T$. The point defects V_{O} and Mo_V are, in turn, shallow donors, which means that they will be easily ionized and produce free electrons in the conduction band of the host material. These results are in agreement with other theoretical reports [18, 20] as well as experimental observations [23].

As described by Eq. (1), the point defect concentration varies with the negative exponential of the formation energy. That is, the lower is the formation energy of a given

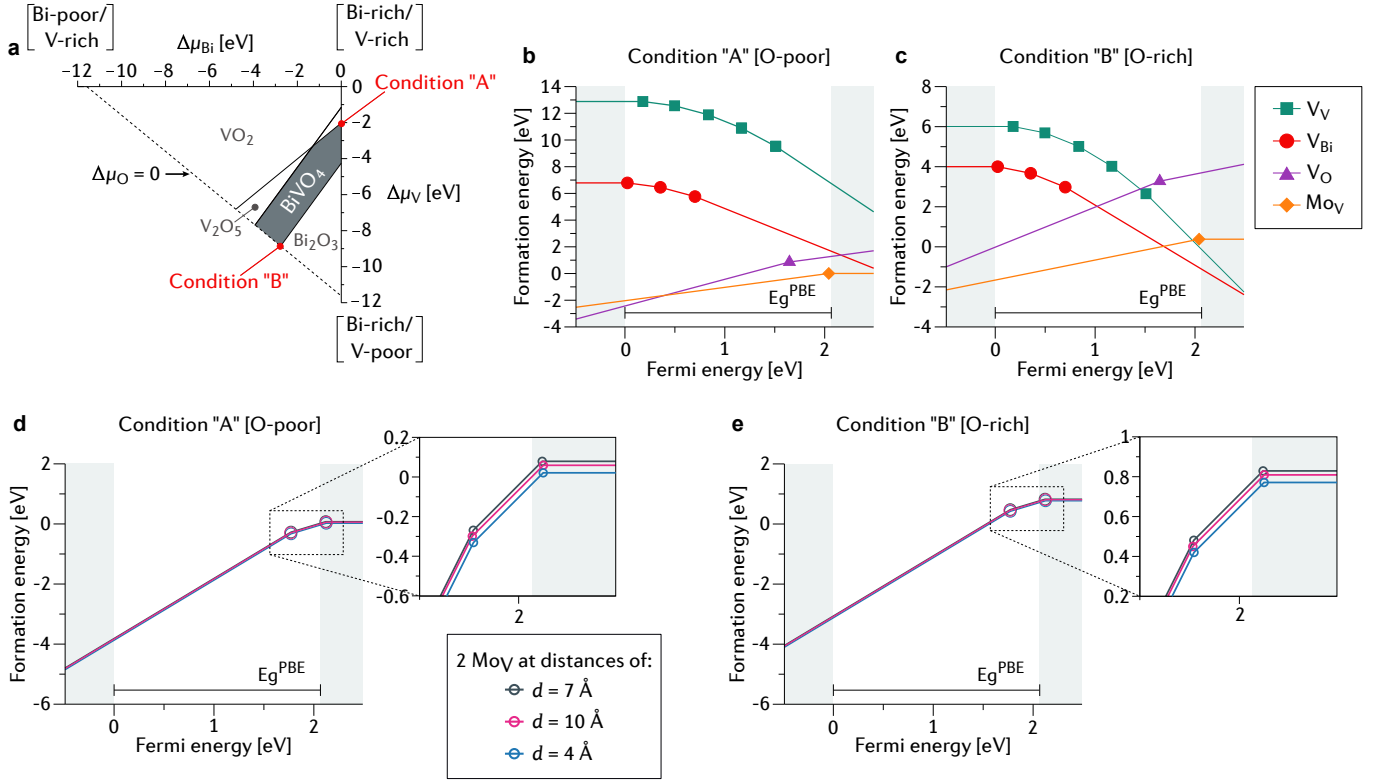


FIG. 3. Accessible range of chemical potentials that stabilize the formation of BiVO_4 and the formation energy of point defects under two growth condition. (a) The stable chemical potential region of BiVO_4 in the $(\Delta\mu_{\text{Bi}}, \Delta\mu_{\text{V}})$ plane with $\Delta\mu_{\text{O}} = 0$ eV (grey area). The conditions “A” (O-poor) and “B” (O-rich) were chosen to numerically represent chemical environments for calculating the formation energy of the point defects. The curves in (b) and (c) show the formation energy of vacancies of vanadium (V_{V}), bismuth (V_{Bi}), oxygen (V_{O}), and single substitutional Mo in V-site (Mo_{V}) under conditions “A” (O-poor) and “B” (O-rich), respectively. In (d) and (e), the plots show the formation energy of pairwise substitutional Mo_{V} defects considering three relative distances of the substitutional sites: 4 Å, 7 Å, and 10 Å, under conditions “A” (O-poor) and “B” (O-rich), respectively.

TABLE I. Transition energies $\epsilon(q/q')$ of Bi, V, and O vacancies, as well as single and pairwise Mo_{V} substitutional defects in BiVO_4 . The energy values were calculated relative to the CBM for the donors, and to the VBM for the acceptors.

Acceptor point defect	$\epsilon(0/-1)$	$\epsilon(-1/-2)$	$\epsilon(-2/-3)$	$\epsilon(-3/-4)$	$\epsilon(-4/-5)$
V_{Bi}	0.02	0.36	0.70		
V_{V}	0.18	0.50	0.84	1.17	1.51
Donor point defect	$\epsilon(0/+1)$	$\epsilon(+1/+2)$	$\epsilon(+2/+3)$	$\epsilon(+3/+4)$	$\epsilon(+4/+5)$
V_{O}	0.42				
Mo_{V}	0.03				
2Mo_{V}	-0.05	0.30			

point defect, the higher will be the prevalence of this defect in the crystal. Thus, considering the expected PEC properties of the Mo-doped BiVO_4 photoanodes, the optimal thermodynamic condition in which we have high concentration of shallow donor defects and low concentration of deep acceptors is depicted by the condition “B”, with an O-poor crystal growing environment. The highest concentration of donor defects in photoanodes introduces larger amounts of free electrons in the conduction

band improving the photoelectrochemical performance. On the other hand, deep levels, known as trap states are detrimental, since they capture photoexcited charge carriers, facilitating electron-hole recombination through Shockley-Read-Hall (trap-assisted) recombination [42].

We also calculated the formation energy of pairs of Mo substitutional defects. $\text{Mo}_{\text{V}}\text{-Mo}_{\text{V}}$ defect pairs are shallow double donors with low formation energies. To investigate the interaction between these defects and the result-

ing variations in their electronic behavior we considered three relative distances ($d_{\text{Mo-Mo}}$): 4 Å, 7 Å, and 10 Å, under the growth conditions “A” (O-poor) and “B” (O-rich) (Figs. 3d and 3e, respectively). Interestingly, the most stable pairwise defect configuration was achieved with the Mo dopants being incorporated into the nearest-neighbor substitutional V-sites, with $d_{\text{Mo-Mo}} = 4$ Å. Seo *et al.* [43] studied the interplay between the N substitutional in O sites (N_O) and oxygen vacancies (V_O) in BiVO_4 , and their results have shown a energetic favorable tendency to form N_O - V_O defect complexes in BiVO_4 . In most of the band gap region, V_O defect exhibits 2+ charge state, whereas N_O defects present mostly 1- charge state. Hence, in this case the electrostatic attraction of the charged point defects can favor the formation of N_O - V_O defect complex.

For the Mo_V - Mo_V pair this result is surprising, since one would expect that the lattice strain induced by the defects would be largest when they are on nearest neighbor sites, leading to a higher formation energy. Similarly, the electrostatic repulsion between the positively charged donors should drive them apart. We observe, however, that the formation energy for the defect complex is the lowest when they are on nearest-neighbor sites. For the intermediate distance configuration, it rises 58 meV (7.5%) and then drops again 20 meV (-2.4%) for the 10 Å separation. This hints to the occurrence of some energy reduction effect associated to hybridization of the electronic clouds of the dopants in close proximity, balancing out the larger repulsion and greater strain of this configuration. As a consequence, this implies a tendency to form Mo_V defect complexes.

A similar behavior for Mo-W codoped BiVO_4 has been reported recently by Pakeetood *et al.* [24]. The authors show that Mo_V - W_V defect complex is more likely to form than Mo_V - V_Bi or W_V - V_Bi , which are both donor-acceptor defects. To date, there is still a lack of physical understanding about these outcomes [44].

In order to understand this unexpected trend, we estimate the local stress field through the difference of the average distance between atoms in the defective and pristine supercell. We used one of the Mo nucleus as the referential, for the defective supercells, and the corresponding V-site as the referential for the pristine supercell. These distances were computed within a cutoff radius of 10.10 Å, considering periodic boundary conditions. The sum of the distances, for the defective and the pristine supercell separately, was averaged by the total number of atoms within the cutoff radius as follows:

$$\langle d \rangle = \sum_{r_{\text{cutoff}}} d_{\text{atom}} / N_{\text{atoms}}, \quad (17)$$

where d_{atom} is the atomic spacing and N_{atoms} is the total number of atoms in each evaluated supercell. Therefore, the local strain was estimated by the difference between $\langle d \rangle$ of the defective ($\langle d \rangle_{2\text{Mo}_\text{V}}$) and pristine ($\langle d \rangle_{\text{pristine}}$) supercells:

$$\langle \Delta d \rangle = \langle d \rangle_{2\text{Mo}_\text{V}} - \langle d \rangle_{\text{pristine}}. \quad (18)$$

Considering only the neutral charge Mo_V defect pair, we obtained $\langle \Delta d \rangle$ equal to 0.072, 0.042, and 0.005 Å/atom for $d_{\text{Mo-Mo}}$ of 4 Å, 7 Å, and 10 Å, respectively. These results of $\langle \Delta d \rangle$ are exactly the same if we considered the charged systems, with $q = 2+$. As expected, we notice that the increase in the separation between the substitutional sites results in a decrease in the local stress. Therefore, lattice strain indeed favors Mo defects farther apart, independently from other effects. As discussed above, we found that the lowest formation energy, however, happens when the two defects are incorporated on neighboring V-sites.

Our findings suggest that electronic effects are at play reducing the enthalpy of formation of the defect complex despite the largest strain and electrostatic repulsion at shortest distance. To test this hypothesis, we first analyzed the charge density differences, which is shown in Fig. 4 (upper panels). Since our purpose is to compare the interaction between the Mo atoms in the three configurations considered, we evaluated the charge distribution as follows:

$$\Delta \rho_{\text{BiVO}_4} = (\rho_{\text{BiVO}_4+2\text{Mo}_\text{V}}) - (\rho_{\text{BiVO}_4} + \rho_{2\text{Mo}} + \rho_{2\text{V}_\text{V}}), \quad (19)$$

in which $\rho_{\text{BiVO}_4+2\text{Mo}_\text{V}}$, ρ_{BiVO_4} , $\rho_{2\text{Mo}}$, and $\rho_{2\text{V}_\text{V}}$ are the charge densities of the BiVO_4 with a pair of Mo_V , the pristine BiVO_4 , the two Mo atoms isolated in the simulation box, and of the BiVO_4 supercell with the V vacancies (Mo incorporation sites), respectively. The $\Delta \rho$ was calculated for the BiVO_4 supercell with a pair of Mo_V defects at distances of 4 Å, 7 Å, and 10 Å from each other. The results were plotted using VESTA code [45].

The excess negative charge due to the Mo_V defects acts as a perturbation of the local charge density distributions, being localized throughout the Mo-O tetrahedrons, with accumulation mainly around the Mo-O bond. We observe electron depletion close to the Mo nuclei. Fig. 4b signalizes hybridization among the orbitals of the two Mo defects, with no indication of nodal points. This is not observed when the Mo defects are farther apart (Fig. 4c and Fig. 4d).

In order to establish on firmer grounds whether electronic hybridization is responsible for the observed tendency of Mo_V to form stable pairs on neighboring sites, we performed a crystal orbital Hamiltonian population (COHP) analyses. The energy-resolved visualization of chemical bonding in BiVO_4 with a pair of Mo_V was generated using the crystal orbital Hamiltonian population (COHP), as implemented in the LOBSTER code [46–49]. This involves a transformation of the plane wave basis set used by VASP, to a localized basis set of Slater-type orbitals (STO) [50]. The projected density of states is defined as:

$$\text{PDOS}_i(E) = \sum_n |c_i^n|^2 \delta(E - E_n), \quad (20)$$

where c_i^n are the coefficients of the molecular orbital expansion regarding the linear combination of atomic or-

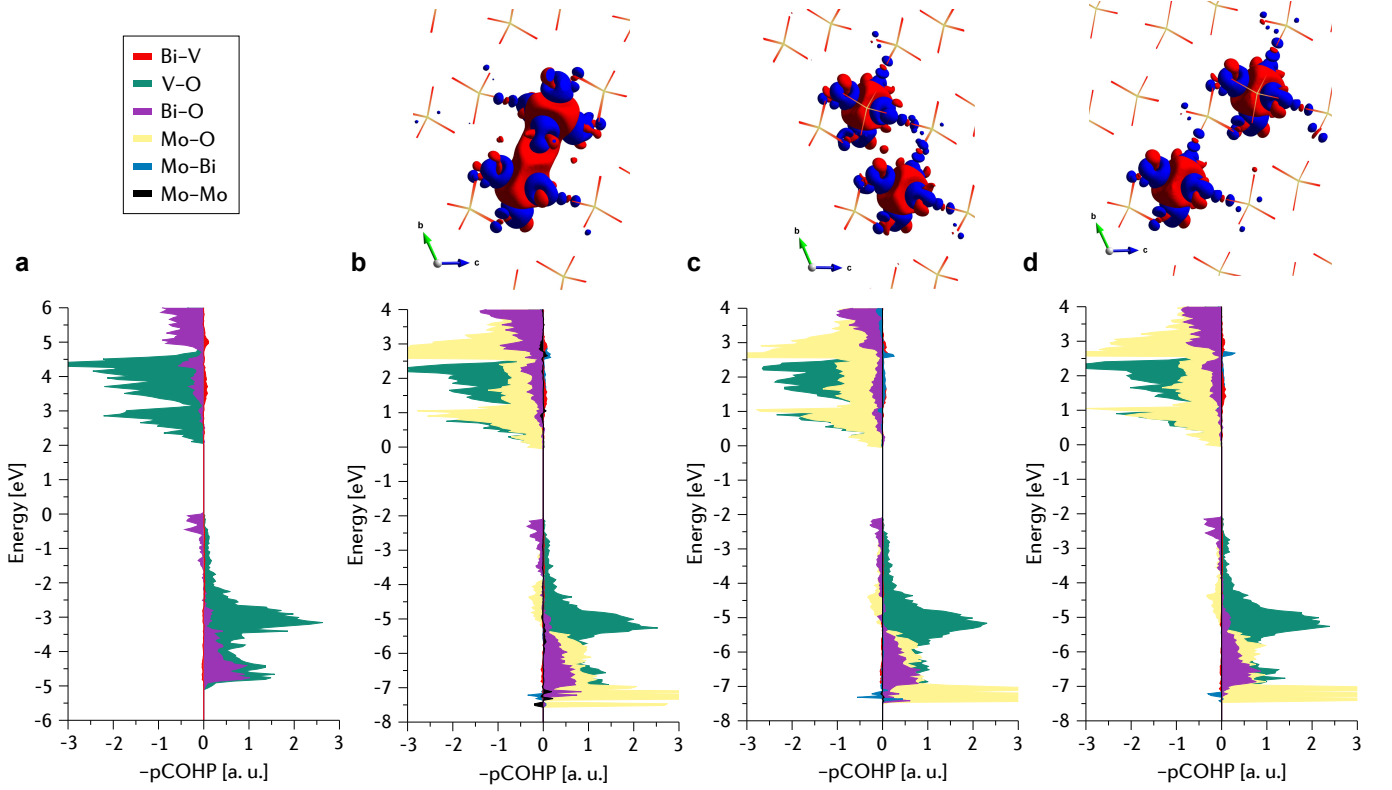


FIG. 4. Crystal orbital hamiltonian populations of (a) BiVO_4 pristine, or containing a double Mo_V defect separated by (b) 4 Å, (c) 7 Å, and (d) 10 Å from each other. The charge density differences for each Mo-Mo relative distances are shown above the respective COHP plots. Blue and red volumes represent electron accumulation and depletion, respectively, with isosurface of $0.005 \text{ e}^- \text{Å}^{-3}$. The Fermi level was set to zero in the energy axes.

TABLE II. Integrated COHP values (in eV) of the respective filled interactions up to the Fermi level for the Mo-related interactions in BiVO_4 with double Mo_V defects in different substitutional-site distances $d_{\text{Mo-Mo}}$.

Interaction	$d_{\text{Mo-Mo}}$		
	4 Å	7 Å	10 Å
Mo-O	2.864	2.734	2.792
Mo-Bi	-0.008	-0.007	-0.008
Mo-Mo	0.005	0.000	0.000

bitals $\psi_n = \sum_i c_i^n \phi_i$. Thus, the COHP is

$$-\text{COHP}_{ij}(E) = H_{ij} \sum_n c_i^n c_j^{*n} \delta(E - E_n), \quad (21)$$

where H_{ij} is the matrix element $\langle \phi_i | H | \phi_j \rangle$ [50]. The minus signal in the Eq. (21) is a mathematical artifact to describe bonding states as positive and anti-bonding states as negative results of the COHP projection. We used the following basis functions for the COHP calculations: Bi $5d6s6p$, V $3d4s$, O $2s2p$, and Mo $4s4p4d5s$, and analyzed the interactions between Bi-V, Bi-O, V-O, Mo-Bi, Mo-O, and Mo-Mo.

The COHP plot of pristine BiVO_4 is shown in Fig. 4a. The curves reveal significant bonding interactions between V and O for the filled electronic states, showing

that the scheelite structure of the BiVO_4 is stabilized mostly by V-O bonds. On the other hand, we see bonding Bi-O interactions at energies around 4 eV below the valence band maximum (VBM). We verify few antibonding states associated to Bi-O interactions near the VBM. Stoltzfus *et al.* [51] performed a study of the structure and bonding in different metal oxides, including BiVO_4 , focusing only on Bi-O interactions. Our COHP results agree with their reports for this interaction. Our analyses also show that the Bi-V interactions do not provide significant bonding/antibonding states in the valence band (Fig. 4a).

In addition, we analyzed the integration of the Mo-related COHP up to the Fermi energy (ICOHP), which can provide useful quantification of Mo-related bond

strength [52, 53]. This furnishes a chemically intuitive interpretation of the electronic structure by comparing bond strength among the different elements in the structure [54]. The results of ICOHP are shown in the Table II, in which the overall bonding and antibonding interactions up to Fermi level are represented by negative and positive values, respectively. We observe a net bonding interaction of the Mo defects pairwise when they are in nearest-neighbor site. The bond strength of the Mo-Mo interaction vanishes when the defect pairs become farther apart. We also observe net anti-bonding states between Mo and Bi atoms which remain on similar levels in all cases. Therefore only in the nearest-neighbor configuration the net anti-bonding interactions are balanced out by Mo pairwise stabilizing interaction.

IV. SUMMARY AND CONCLUSIONS

In summary, we investigated by first-principles calculations the electronic nature and the interaction between substitutional Mo defects in Mo-doped BiVO_4 . Our analyses indicated that these shallow donors, that have been shown to enhance the photoelectrochemical performance of the material, display an unexpected inflection in their

formation energy versus their relative distance curve. The most favorable configuration for Mo_V defect pairs in BiVO_4 is when they are on nearest-neighbor sites, despite the electrostatic repulsion they exert on each other. Our simulations also confirm that the lattice is more strained when the defects are on nearest-neighbor sites. This is also at odds with the observed lowest formation energy for this configuration. The COHP analyses showed that only in the nearest-neighbor configuration bonding states exist between the two Mo atoms, balancing out the electrostatic repulsion and lattice strain that would favor configurations with the defects farther apart. Our findings indicate that BiVO_4 doped with Mo tends to form defect clusters, pointing out to new research issues that can improve the photoactivity of these metal oxides.

V. ACKNOWLEDGMENTS

This work was supported by the Brazilian Federal Agency for Support and Evaluation of Graduate Education (CAPES). We thank Lídia Carvalho Gomes and Juan Camilo Alvarez Quiceno for fruitful discussions. Computational resources were provided by the high performance computing center at UFABC.

-
- [1] A. Fujishima and K. Honda, Electrochemical photolysis of water at a semiconductor electrode, *Nature* **238**, 37 (1972).
 - [2] J. K. Cooper, S. B. Scott, Y. Ling, J. Yang, S. Hao, Y. Li, F. M. Toma, M. Stutzmann, K. V. Lakshmi, and I. D. Sharp, Role of hydrogen in defining the n-type character of BiVO_4 photoanodes, *Chemistry of Materials* **28**, 5761 (2016).
 - [3] Y. Yang, S. Niu, D. Han, T. Liu, G. Wang, and Y. Li, Progress in developing metal oxide nanomaterials for photoelectrochemical water splitting, *Advanced Energy Materials* **7**, 1700555 (2017).
 - [4] F. F. Abdi and S. P. Berglund, Recent developments in complex metal oxide photoelectrodes, *Journal of Physics D: Applied Physics* **50**, 193002 (2017).
 - [5] A. Kudo, K. Ueda, H. Kato, and I. Mikami, Photocatalytic O_2 evolution under visible light irradiation on BiVO_4 in aqueous AgNO_3 solution, *Catalysis Letters* **53**, 229 (1998).
 - [6] F. F. Abdi, N. Firet, and R. van de Krol, Efficient BiVO_4 thin film photoanodes modified with cobalt phosphate catalyst and W-doping, *ChemCatChem* **5**, 490 (2013).
 - [7] A. Kudo, K. Omori, and H. Kato, A novel aqueous process for preparation of crystal form-controlled and highly crystalline BiVO_4 powder from layered vanadates at room temperature and its photocatalytic and photophysical properties, *Journal of the American Chemical Society* **121**, 11459 (1999).
 - [8] J. K. Cooper, S. Gul, F. M. Toma, L. Chen, Y. S. Liu, J. Guo, J. W. Ager, J. Yano, and I. D. Sharp, Indirect bandgap and optical properties of monoclinic bismuth vanadate, *The Journal of Physical Chemistry C* **119**, 2969 (2015).
 - [9] A. Walsh, Y. Yan, M. N. Huda, M. M. Al-Jassim, and S. H. Wei, Band edge electronic structure of BiVO_4 : elucidating the role of the Bi s and V d orbitals, *Chemistry of Materials* **21**, 547 (2009).
 - [10] K. Sivula and R. Van De Krol, Semiconducting materials for photoelectrochemical energy conversion, *Nature Reviews Materials* **1**, 15010 (2016).
 - [11] Y. Zhao, R. Li, L. Mu, and C. Li, Significance of crystal morphology controlling in semiconductor-based photocatalysis: a case study on BiVO_4 photocatalyst, *Crystal Growth & Design* **17**, 2923 (2017).
 - [12] K. H. Ye, H. Li, D. Huang, S. Xiao, W. Qiu, M. Li, Y. Hu, W. Mai, H. Ji, and S. Yang, Enhancing photoelectrochemical water splitting by combining work function tuning and heterojunction engineering, *Nature Communications* **10**, 1 (2019).
 - [13] Z. He, Y. Shi, C. Gao, L. Wen, J. Chen, and S. Song, BiOCl/BiVO_4 p-n heterojunction with enhanced photocatalytic activity under visible-light irradiation, *The Journal of Physical Chemistry C* **118**, 389 (2014).
 - [14] F. F. Abdi, L. Han, A. H. Smets, M. Zeman, B. Dam, and R. Van De Krol, Efficient solar water splitting by enhanced charge separation in a bismuth vanadate-silicon tandem photoelectrode, *Nature Communications* **4**, 2195 (2013).
 - [15] T. W. Kim and K. S. Choi, Nanoporous BiVO_4 photoanodes with dual-layer oxygen evolution catalysts for solar water splitting, *Science* **343**, 990 (2014).
 - [16] F. F. Abdi and R. van de Krol, Nature and light dependence of bulk recombination in Co-Pi-catalyzed BiVO_4 photoanodes,

- The Journal of Physical Chemistry C **116**, 9398 (2012).
- [17] K. P. S. Parmar, H. J. Kang, A. Bist, P. Dua, J. S. Jang, and J. S. Lee, Photocatalytic and photoelectrochemical water oxidation over metal-doped monoclinic BiVO_4 photoanodes, *ChemSusChem* **5**, 1926 (2012).
 - [18] G. Wang, Y. Ling, X. Lu, F. Qian, Y. Tong, J. Z. Zhang, V. Lordi, C. Rocha Leão, and Y. Li, Computational and photoelectrochemical study of hydrogenated bismuth vanadate, *The Journal of Physical Chemistry C* **117**, 10957 (2013).
 - [19] T. W. Kim, Y. Ping, G. A. Galli, and K. S. Choi, Simultaneous enhancements in photon absorption and charge transport of bismuth vanadate photoanodes for solar water splitting, *Nature Communications* **6**, 8769 (2015).
 - [20] W. J. Yin, S. H. Wei, M. M. Al-Jassim, J. Turner, and Y. Yan, Doping properties of monoclinic BiVO_4 studied by first-principles density-functional theory, *Physical Review B* **83**, 155102 (2011).
 - [21] H. S. Park, K. E. Kweon, H. Ye, E. Paek, G. S. Hwang, and A. J. Bard, Factors in the metal doping of BiVO_4 for improved photoelectrocatalytic activity as studied by scanning electrochemical microscopy and first-principles density-functional calculation, *The Journal of Physical Chemistry C* **115**, 17870 (2011).
 - [22] W. Luo, J. Wang, X. Zhao, Z. Zhao, Z. Li, and Z. Zou, Formation energy and photoelectrochemical properties of bivo 4 after doping at bi 3+ or v 5+ sites with higher valence metal ions, *Physical Chemistry Chemical Physics* **15**, 1006 (2013).
 - [23] H. W. Jeong, T. H. Jeon, J. S. Jang, W. Choi, and H. Park, Strategic modification of BiVO_4 for improving photoelectrochemical water oxidation performance, *The Journal of Physical Chemistry C* **117**, 9104 (2013).
 - [24] P. Pakeetood, P. Reunchan, A. Boonchun, S. Limpijumnong, R. Munprom, R. Ahuja, and J. T-Thienprasert, Hybrid-functional study of native defects and W/Mo-doped in monoclinic-bismuth vanadate, *The Journal of Physical Chemistry C* **123**, 14508 (2019).
 - [25] P. Hohenberg and W. Kohn, Inhomogeneous electron gas, *Physical Review* **136**, B864 (1964).
 - [26] W. Kohn and L. J. Sham, Self-consistent equations including exchange and correlation effects, *Physical Review* **140**, A1133 (1965).
 - [27] G. Kresse and J. Furthmüller, Efficient iterative schemes for ab initio total-energy calculations using a plane-wave basis set, *Physical Review B* **54**, 11169 (1996).
 - [28] P. E. Blöchl, Projector augmented-wave method, *Physical Review B* **50**, 17953 (1994).
 - [29] J. P. Perdew, K. Burke, and M. Ernzerhof, Generalized gradient approximation made simple, *Physical Review Letters* **77**, 3865 (1996).
 - [30] L. J. Cheng, C. J. Ping, and L. D. Yu, Crystal structure and optical observations of BiVO_4 , *Acta Physica Sinica* **32**, 1053 (1983).
 - [31] H. J. Monkhorst and J. D. Pack, Special points for brillouin-zone integrations, *Physical Review B* **13**, 5188 (1976).
 - [32] A. J. E. Rettie, H. C. Lee, L. G. Marshall, J. F. Lin, C. Capan, J. Lindemuth, J. S. McCloy, J. Zhou, A. J. Bard, and C. B. Mullins, Combined charge carrier transport and photoelectrochemical characterization of BiVO_4 single crystals: intrinsic behavior of a complex metal oxide, *Journal of the American Chemical Society* **135**, 11389 (2013).
 - [33] J. K. Cooper, S. Gul, F. M. Toma, L. Chen, P.-A. Glans, J. Guo, J. W. Ager, J. Yano, and I. D. Sharp, Electronic structure of monoclinic bivo4, *Chemistry of Materials* **26**, 5365 (2014).
 - [34] P. A. Varotsos and K. D. Alexopoulos, *Thermodynamics of point defects and their relation with bulk properties* (Elsevier Science, 2013).
 - [35] H. P. Komsa, T. T. Rantala, and A. Pasquarello, Finite-size supercell correction schemes for charged defect calculations, *Physical Review B* **86**, 045112 (2012).
 - [36] C. Rocha Leão and V. Lordi, Ab initio guided optimization of GaTe for radiation detection applications, *Physical Review B* **84**, 165206 (2011).
 - [37] G. Makov and M. C. Payne, Periodic boundary conditions in ab initio calculations, *Physical Review B* **51**, 4014 (1995).
 - [38] Z. Zhao, Z. Li, and Z. Zou, Electronic structure and optical properties of monoclinic clinobisvanite BiVO_4 , *Physical Chemistry Chemical Physics* **13**, 4746 (2011).
 - [39] S. Lany and A. Zunger, Assessment of correction methods for the band-gap problem and for finite-size effects in supercell defect calculations: Case studies for zno and gaas, *Physical Review B* **78**, 235104 (2008).
 - [40] S. Lany and A. Zunger, Accurate prediction of defect properties in density functional supercell calculations, *Modelling and Simulation in Materials Science and Engineering* **17**,
 - [41] C. Persson, Y. J. Zhao, S. Lany, and A. Zunger, n-Type doping of CuInSe_2 and CuGaSe_2 , *Physical Review B* **72**, 035211 (2005), 1504.06521.
 - [42] J. S. Park, S. Kim, Z. Xie, and A. Walsh, Point defect engineering in thin-film solar cells, *Nature Reviews Materials* **3**, 194 (2018).
 - [43] H. Seo, Y. Ping, and G. Galli, Role of point defects in enhancing the conductivity of BiVO_4 , *Chemistry of Materials* **30**, 7793 (2018).
 - [44] For completeness, we also calculate the formation energy of W_V defect pairs, considering the same relative distances of the substitutional sites: 4 Å, 7 Å, and 10 Å. The W 5p5d6s electrons were treated as valence electrons. We observe identical behavior for W_V embedded in nearest-neighbor V-sites. Regarding the neutral charged BiVO_4 with pairs of W_V , for O-poor growth condition, we obtain $\Delta H_f = 0.68, 0.74, \text{ and } 0.72$ eV for relative distances of 4 Å, 7 Å, and 10 Å, respectively. Similarly, for O-rich growth condition, we obtain $\Delta H_f = 1.39, 1.45, \text{ and } 1.43$ eV for 4 Å, 7 Å, and 10 Å, respectively.
 - [45] K. Momma and F. Izumi, *VESTA 3* for three-dimensional visualization of crystal, volumetric and morphology data, *Journal of Applied Crystallography* **44**, 1272 (2011).
 - [46] S. Maintz, V. L. Deringer, A. L. Tchougréeff, and R. Dronskowski, Lobster: A tool to extract chemical bonding from plane-wave based dft, *Journal of Computational Chemistry* **37**, 1030 (2016).
 - [47] R. Dronskowski and P. E. Blochl, Crystal orbital Hamilton populations (COHP): energy-resolved visualization of chemical bonding in solids based on density-functional calculations, *The Journal of Physical Chemistry* **97**, 8617 (1993).
 - [48] V. L. Deringer, A. L. Tchougréeff, and R. Dronskowski, Crystal orbital Hamilton population (COHP) analysis as projected from plane-wave basis sets, *The Journal of Physical Chemistry A* **115**, 5461 (2011).

- [49] S. Maintz, V. L. Deringer, A. L. Tchougréeff, and R. Dronskowski, Analytic projection from plane-wave and paw wavefunctions and application to chemical-bonding analysis in solids, *Journal of Computational Chemistry* **34**, 2557 (2013).
- [50] S. Tao, I. Schmidt, G. Brocks, J. Jiang, I. Tranca, K. Meerholz, and S. Olthof, Absolute energy level positions in tin-and lead-based halide perovskites, *Nature Communications* **10**, 2560 (2019).
- [51] M. W. Stoltzfus, P. M. Woodward, R. Seshadri, J. H. Klepeis, and B. Bursten, Structure and bonding in SnWO_4 , PbWO_4 , and BiVO_4 : lone pairs vs inert pairs, *Inorganic Chemistry* **46**, 3839 (2007).
- [52] D. K. Mann, J. Xu, N. E. Mordvinova, V. Yannello, Y. Ziouani, N. González-Ballesteros, J. P. Sousa, O. I. Lebedev, Y. V. Kolen'ko, and M. Shatruk, Electrocatalytic water oxidation over AlFe_2B_2 , *Chemical Science* **10**, 2796 (2019).
- [53] M. Khazaei, J. Wang, M. Estili, A. Ranjbar, S. Suehara, M. Arai, K. Esfarjani, and S. Yunoki, Novel MAB phases and insights into their exfoliation into 2D MBenes, *Nanoscale* **11**, 11305 (2019).
- [54] B. R. Ortiz, L. C. Gomes, J. R. Morey, M. Winiarski, M. Bordelon, J. S. Mangum, I. W. H. Oswald, J. A. Rodriguez-Rivera, J. R. Neilson, S. D. Wilson, E. Ertekin, T. M. McQueen, and E. S. Toberer, New kagome prototype materials: discovery of KV_3Sb_5 , RbV_3Sb_5 , and CsV_3Sb_5 , *Physical Review Materials* **3**, 094407 (2019).